Article

Micromechanical Dilution of PLA/PETG−Glass/Iron Nanocomposites: A More Efficient Molecular Dynamics Approach

William A. Pisani, Dane N. Wedgeworth, Jedadiah F. Burroughs, Travis L. Thornell, J. Kent Newman, and Manoj K. Shukla*

Cite This: *ACS Omega* 2024, 9, 14887−14898

Read Online

ACCESS | Metrics & More | Article Recommendations | Supporting Information

ABSTRACT: Polylactic acid (PLA) and poly(ethylene terephthalate glycol) (PETG) are popular thermoplastics used in additive manufacturing applications. The mechanical properties of PLA and PETG can be significantly improved by introducing fillers, such as glass and iron nanoparticles (NPs), into the polymer matrix. Molecular dynamics (MD) simulations with the reactive INTERFACE force field were used to predict the mechanical responses of neat PLA/PETG and PLA−glass/iron and PETG−glass/iron nanocomposites with relatively high loadings of glass/iron NPs. We found that the iron and glass NPs significantly increased the elastic moduli of the PLA matrix, while the PETG matrix exhibited modest increases in elastic moduli. This difference in reinforcement ability may be due to the slightly greater attraction between the glass/iron NP and PLA matrix. The NASA Multiscale Analysis Tool was used to predict the mechanical response across a range of volume percent glass/iron filler by using only the neat and highly loaded MD predictions as input. This provides a faster and more efficient approach than creating multiple MD models per volume percent per polymer/filler combination. To validate the micromechanics predictions, experimental samples incorporating hollow glass microspheres (MS) and carbonyl iron particles (CIP) into PLA/PETG were developed and tested for elastic modulus. The CIP produced a larger reinforcement in elastic modulus than the MS, with similar increases in elastic modulus between PLA/CIP and PETG/CIP at 7.77 vol % CIP. The micromechanics-based mechanical predictions compare excellently with the experimental values, validating the integrated micromechanical/MD simulation-based approach.

NASMAT
NASA Multiscale Analysis Tool
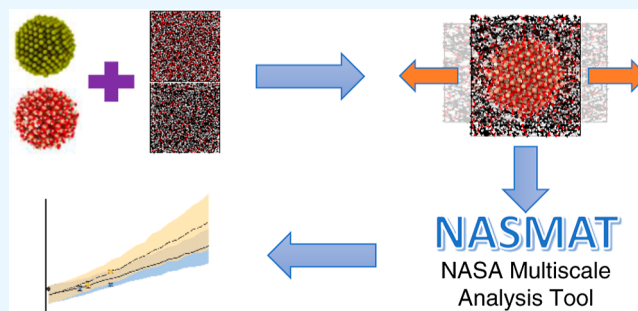
INTRODUCTION

Polylactic acid (PLA) and polyethylene terephthalate glycol (PETG) are popular thermoplastics used in additive manufacturing (3D printing) applications.[1−16] PLA is commonly used as a 3D printing filament due to its processability, biodegradability, compostability, and recyclability.[17−21] PETG is widely used in 3D printing due to its flexibility, processability, and good chemical, moisture, and UV resistance.[1,2,12−15] The mechanical properties of PLA and PETG can be significantly improved by introducing fillers into the polymer matrix. The resulting polymer composites can be manufactured into production-ready 3D printing filaments.[15,22] Glass beads and iron particles have previously been used in 3D printing filaments with success.[23−27]

Glass has been used as a mechanical reinforcement in polymers for decades as both fibers and hollow/solid glass beads.[28−31] Glass beads have been used as a filler in PLA to improve various properties including fire safety,[32] thermal insulation,[33] elastic modulus and thermal decomposition temperature,[34] and compression strength and acoustic insulation.[35] Glass fibers have been used in PETG for 3D printing applications,[36] but, to our knowledge, glass beads have

not been used in PETG. Carbonyl iron particles (CIP) are mainly used in applications that take advantage of their magnetism such as electromagnetic interference shielding and medical treatments.[24−27,37−41] However, CIP can also be used to improve the thermo-mechanical properties of the polymer matrix.[42] CIP have been used in PETG for electromagnetic interference shielding[25] but, to our knowledge, have not been used in PETG or PLA as a mechanical reinforcement. Glass beads and CIP were chosen as fillers in this work because the mechanical responses of PLA/CIP, PETG/glass, and PETG/CIP have not yet been explored. PLA with glass beads has been investigated as a foam composite,[34] but not as a solid. Thus, we included PLA/glass as well in the current investigation.
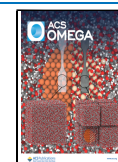
Molecular dynamics (MD) simulations are widely used for predicting thermo-mechanical properties of polymers and

polymer composites.[43−63] MD simulations have proven to be accurate, efficient, trustworthy, and quite capable of exploring the structure−property relationships of polymer composites. With MD, atoms are simulated according to Newton's laws of motion combined with "force fields" that define how the atoms interact with each other. An MD simulation is only as accurate as the force field. The INTERFACE force field (IFF) and IFF reactive version (IFF-R) produce accurate predictions of thermal, mechanical, and interfacial properties of polymer composites.[43,44,49,50,54,56,58,63−67]

In this study, we explored the structure−property relationships of PLA and PETG glass/iron nanocomposites at 20 volume percent (vol %) glass/iron. Our goal was to understand how the mechanical properties of the PLA/PETG−glass/iron nanocomposites change as the volume percent of glass/iron increases from 0 to 20 vol %. However, creating multiple MD models per vol % per polymer/filler combination quickly becomes impractical due to time and computational resource constraints. However, it is possible to use a micromechanics approach to predict mechanical properties as a function of vol % filler using the MD predictions as input.[55,59] The NASA Multiscale Analysis Tool (NASMAT)[68,69] uses accurate and efficient micromechanical theory.[70,71] NASMAT is the successor to and is based on MAC/GMC micromechanics software developed by the NASA Glenn Research Center. The micromechanics theory underpinning NASMAT and MAC/GMC have been validated multiple times.[44,46,55,57,59,60,62,69] Additionally, the use of micromechanics via NASMAT and MAC/GMC can effectively "scale up" MD results to the macroscale, thus eliminating the need to simulate experimental-size glass beads or CIP.[72]

In the following sections, we describe the procedure for establishing and testing well-equilibrated, polymerized neat PLA/PETG and PLA/PETG−iron/glass nanocomposite MD models. The micromechanics approach with NASMAT is detailed, and the experimental manufacture and testing of the PLA/PETG−CIP/hollow glass bead composites are described. The experimental mechanical response is then discussed. The strength of the PLA/PETG−iron/glass interface is discussed in terms of MD interaction energy. The MD mechanical response is discussed. Finally, the micromechanical predictions as a function of iron/glass are compared with experimental results for validation. The micromechanical predictions compare excellently with the experimental values, validating the micromechanical dilution approach.

■ THEORETICAL METHODS

The open-source MD code LAMMPS[73,74] was used to perform all MD simulations (1 fs time step). Detailed methodologies for constructing all of the MD polymers and nanocomposites are given in the Supporting Information. Unless otherwise noted, all molecular visualizations were rendered with the OVITO software.[75] The class2 IFF[64,65] was used to construct the MD models. IFF is well-known for accurately predicting interfacial properties of polymer nanocomposites.[43,49,50,56,58] However, IFF is a fixed-bond force field and is fundamentally incapable of accurately simulating large deformations. IFF was extended with the Morse potential in 2021[66] to enable bond scission, thus allowing IFF to accurately simulate large deformation. This hybrid class2/Morse force field is called IFF-R (IFF Reactive version), and it was used in this study for the prediction of the mechanical properties.

Neat PLA and PETG. A PLA trimer and a PETG monomer were constructed and parameterized in the IFF using in-house BASH/Python tools. The molecular structures of the PLA trimer and PETG monomer are shown in Figures 1 and 2,
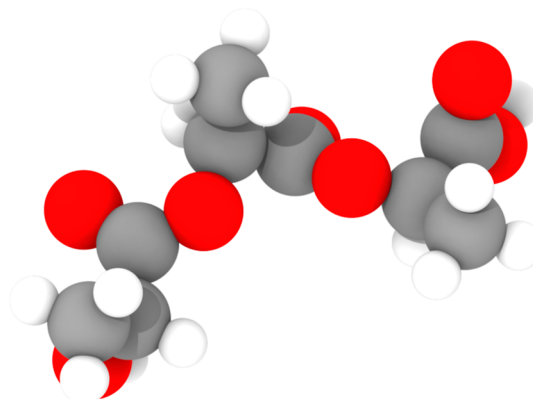

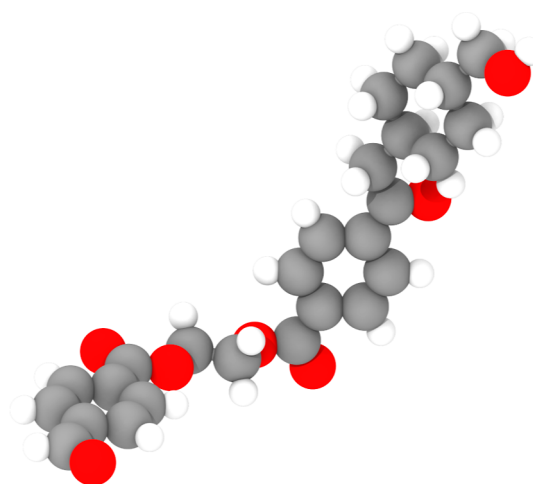**Figure 1.** PLA trimer molecular structure as used in this work.

Figure 2. PETG molecular structure as used in this work.

respectively. The REACTER protocol[76,77] as implemented in LAMMPS was used for polymerization. For PLA, a trimer was chosen because the trimer molecule is long enough that the REACTER protocol can be easily used without length issues. The energy of the PLA trimer and PETG monomer was minimized using the conjugate gradient algorithm (Polak−Ribiere version) with an energy tolerance of 1×10^{-4} (unitless), a force tolerance of 1×10^{-6} (kcal/mol Å), a maximum iteration of 1000, and a maximum force/energy evaluation of 10,000. After minimization, each trimer/monomer was simulated at 300 K for 3 ns by using the NVT ensemble (N is the constant number of particles, V is the constant volume, and T is the constant temperature) to equilibrate the structure.

Ten neat PLA replicates and ten neat PETG replicates were established in IFF. The neat PLA systems initially contained 24,960 atoms (832 trimers), and the neat PETG systems initially contained 25,620 atoms (420 monomers). Each PLA replicate started in a gaseous state and was densified in a high-temperature three-stage process: (1) temperature ramp from 300 to 500 K with NVT over 100 ps; (2) NPT (N is the constant number of particles, P is the constant pressure, and T is the constant temperature) (iso keyword) at 500 K and 1.0

atm for 200 ps to rapidly shrink the simulation box; and (3) densify to a bulk density of 1.187 g cm^{-3} at a rate of 20 Å ns^{-1}. This density was chosen such that the final equilibrated density would be close to the experimental density of 1.242 g cm^{-3}. Please see Supporting Information for more discussion. The PETG replicates were densified similarly, but with a few changes: (1) temperature was set to 300 K; (2) the NVT and NPT runs were increased to 400 and 500 ps, respectively, to account for the significantly larger molecule; and (3) the bulk density was 1.27 g cm^{-3}. The PLA systems were densified at 500 K rather than 300 K because they were more prone to the formation of void space, and the higher temperature reduced the formation of voids considerably. After densification, long-range Coulombic interactions were enabled with a Lennard-Jones and Coulombic cutoff of 10.0 Å, and the PLA/PETG replicates were then polymerized similarly using the REAC-TER protocol. Please see Supporting Information for the complete list of REACTER parameters used. PLA used NVT, while PETG used the NPT ensemble with the aniso keyword. The PLA replicates were polymerized at 350 K and 1.0 atm, while the PETG replicates were polymerized at 600 K and 1.0 atm (both for 1 ns); these conditions were used for the greatest extents of polymerization. PLA undergoes a linear polycondensation reaction, which produces a water molecule every time two PLA molecules bond. In this work, the water molecules were immediately deleted after forming using the deleteIDs keyword in the REACTER mapping file to simulate a fully dried material. When PETG molecules bond, a hydrogen molecule is produced. Similarly to PLA, these hydrogen molecules were deleted to simulate a fully off-gassed material. For PLA, the average extent of polymerization was 90% ± 0.73%, while for PETG, the average extent of polymerization was 92% ± 0.90%. Please see Table S1 for molecular weight information on the neat PLA and PETG MD samples.

The polymerized systems were then equilibrated for 4 ns using NPT (aniso keyword) at 300 K and 1.0 atm. The anisotropic barostat is used to allow the systems to fully relax in each Cartesian axis. The analysis of potential energy monitoring, density profiling, and explicit residual stress checking revealed that the system relaxed within 1 ns, and simulated systems are well-equilibrated. An explicit check for residual stresses was conducted on the polymerized, equilibrated systems; residual stresses were negligible. Figure 3 shows the xz-plane of two equilibrated, polymerized MD models of neat PLA and PETG. The average PLA and PETG densities in our simulations were found to be 1.246 ± 0.010 g
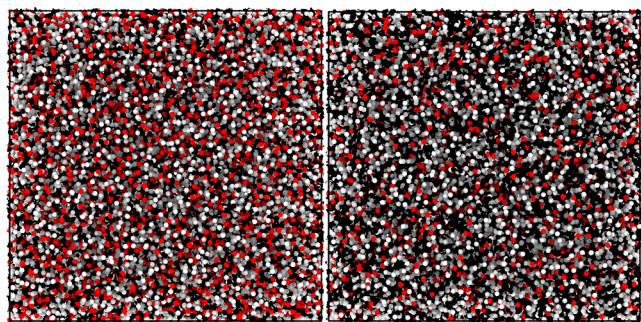

Figure 3. Representative MD models of PLA (left) and PETG (right).

cm^{-3} and 1.2386 ± 0.0014 g cm^{-3}, respectively. The predicted PLA density compares excellently with the experimental value of 1.242 g cm^{-3}, while the predicted PETG density compares moderately well with the experimental value of 1.335 g cm^{-3}. Please note that the density of PETG ranges from 1.18 to 1.37 g cm^{-3}.[78] Therefore, we started our simulation of PETG with an average density of 1.27 g cm^{-3}. Additionally, given that the predicted mechanical properties of PETG compare well with the experiment (as seen later in the Results and Discussion section), we can say that the relative mismatch between predicted and experimental PETG density is acceptable.

Glass and Iron Nanoparticles. The 31 Å diameter hydrogen-terminated glass nanoparticle (NP) was carved out of a bulk quartz crystal[79] using Python and the Atomic Simulation Environment (ASE) library.[80] The molecular topology was added according to Sorkin et al.;[81] please see the Supporting Information for more details. The NP (1595 atoms) was parameterized in IFF using an in-house Python script. The parameterized NP was minimized using the conjugate gradient algorithm (Polak−Ribiere version) with an energy tolerance of 1×10^{-4} (unitless), a force tolerance of 1×10^{-6} (kcal/mol Å), a maximum iteration of 1000, and a maximum force/energy evaluation of 10,000. The velocity distribution was set to 300 K, and the NP was run for 100 ps with NVT at 300 K to ensure stability. The glass NPs are shown in Figure 4a. It is important to note that the MD glass
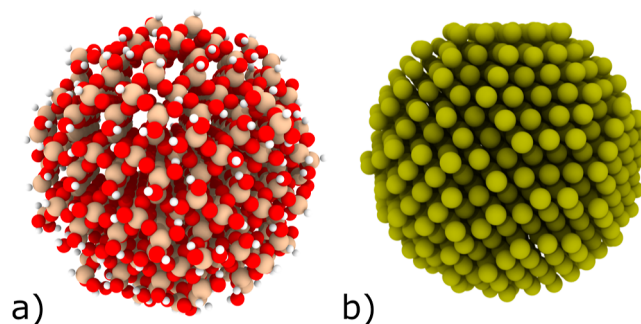

Figure 4. Glass (a) and iron (b) NPs used in this work.

NP was created as a solid to conserve computational resources. A hollow MD glass NP would need to be significantly larger for the hollowness to appropriately affect the MD simulations.

The 32 Å diameter iron NP (1513 atoms) was carved out of a bulk FCC (100) iron crystal created with ASE and then assigned IFF-compatible Lennard-Jones parameters.[82] The iron NP is shown in Figure 4b. This iron NP was not minimized or simulated prior to insertion into the polymer systems due to the simpler parameters. It is important to note that iron at room temperature is in the BCC crystal structure, but the BCC crystal structure is unavailable for iron in IFF.[82] It is currently possible to use iron in the BCC structure with IFF only if the initial BCC atom positions are fixed in space (thus holding the BCC structure in place), but this usage will not allow for deformation upon load transfer, resulting in unrealistic predictions. While BCC iron is available in other force fields, such as the embedded atom model, we chose IFF for simplicity. Covering the surface of the iron NP with an oxide layer would be most realistic, but iron oxide is also not yet available in IFF. Still, even with these caveats, the PLA/PETG−iron predictions match well with the experiment.

PLA/PETG−Glass/Iron Nanocomposites. The target volume percent of reinforcement for the PLA/PETG nanocomposites was 20% glass/iron. This target volume percent was chosen to conserve computational resources, as a larger amount of glass/iron would necessarily require fewer amounts of polymer molecules. Also, a larger target volume percent would allow for a larger range of volume percent after dilution with neat polymer using micromechanics, which would be more helpful to the composite community than a smaller range. Ten replicates of PLA−glass, PLA−iron, PETG−glass, and PETG−iron (total of 40 replicates) were established in IFF. The required number of equilibrated PLA and PETG molecules (315 PLA molecules−9450 atoms, 144 PETG molecules−8784 atoms) needed to achieve 20% by volume glass/iron PLA/PETG nanocomposites after polymerization (85% PLA, 90% PETG) were placed into a simulation box in a gaseous state. The replicates were then densified to the PLA/PETG bulk densities according to the same methodology as the neat polymers. After densification, a spherical indentation (using the "fix indent" LAMMPS command) was created gradually from zero to 40 Å in diameter over 10 ps with *NVT* at 300 K. These indented systems were used for both glass and iron NPs. After indentation, the glass-iron NP was inserted into the center of the spherical void. To prevent the system from immediately drifting, the linear momentum was zeroed. The systems were then run for 50 ps under *NVE*, but each atom was limited to moving a maximum distance of 0.1 Å per time step. If any atoms were overlapped as a result of inserting the glass/iron NP, then *NVE* with a limiter would resolve the overlap safely. The systems were run with *NVT* at 300 K for 100 ps and finally *NPT* (iso keyword) at 300 K and 1.0 atm for 500 ps in a brief equilibration.

After indentation and insertion of the NP, long-range Coulombic interactions were enabled with a Lennard-Jones and Coulombic cutoff of 10.0 Å, and then each system was polymerized by using the REACTER protocol. The REACTER settings of the polymer nanocomposites were the same as those of the respective matrix polymer. Please see the Supporting Information for the complete list of REACTER protocols. The nanocomposites were polymerized over 1 ns using the *NPT* ensemble (aniso keyword) to set the pressure and temperature. The average extents of polymerization for the PLA/glass and PLA/iron nanocomposites were 86% ± 1.4% and 84% ± 1.2%, respectively. The average extents of polymerization for the PETG/glass and PETG/iron nanocomposites were 92% ± 1.1% and 86% ± 2.4%, respectively. Please see Table S1 for molecular weight information on the PLA−glass/iron and PETG−glass/iron MD samples.

The polymerized PLA/PETG−glass/iron systems were then equilibrated for 2 ns under *NPT* (aniso keyword) at 300 K and 1.0 atm. The anisotropic barostat is used to allow the systems to fully relax in each Cartesian axis. The analysis of potential energy monitoring, density profiling, and explicit residual stress checking revealed that system relaxed within 1 ns and simulated systems are well-equilibrated. An explicit check for residual stresses was conducted on the polymerized, equilibrated systems; residual stresses were negligible. Figure 5 shows the *xz*-plane of the two equilibrated polymerized MD models of PLA/iron and PETG/glass. The average densities of the PLA−glass/iron nanocomposites were 1.5224 ± 0.0029 g cm⁻³ and 2.4417 ± 0.0067 g cm⁻³, respectively. The average densities of the PETG−glass/iron nanocomposites were 1.4411 ± 0.0053 g cm⁻³ and 2.3506 ± 0.0060 g cm⁻³,
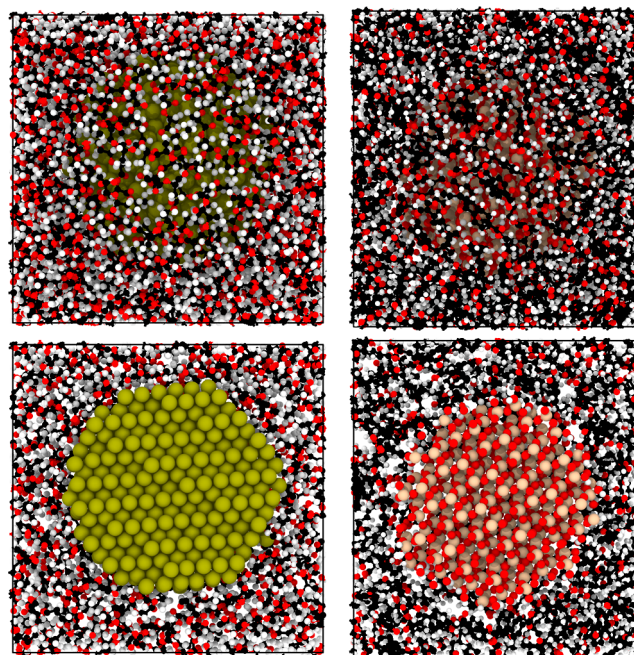

Figure 5. Representative MD models of PLA/iron (left) and PETG/glass (right) nanocomposites. The top view shows the outside of the MD model, while the bottom view shows a slice through the center of the composites.

respectively. After equilibration, the interaction energy between the PLA/PETG matrix and glass/iron reinforcement was measured using the LAMMPS "compute group/group" command over 500 ps under the *NPT* (aniso keyword) ensemble at 300 K and 1.0 atm. The interaction energy values reported in this work are a result of a running average over every time step of the 500 ps simulation time. It is important to note that the final volume percentages of the PLA/PETG− glass/iron systems drifted from 20 vol %. Table 1 shows the final loadings of the PLA/PETG−glass/iron MD nanocomposites in terms of volume and mass percent.

Table 1. PLA/PETG−Glass/Iron MD Nanocomposite Loading in Mass and Volume Percent

polymer	filler	volume, %	mass, %
PLA	iron	16.66 ± 0.04	55.04 ± 0.02
PLA	glass	21.72 ± 0.29	27.95 ± 0.02
PETG	iron	16.47 ± 0.06	56.55 ± 0.00
PETG	glass	21.66 ± 0.43	29.17 ± 0.00

MD Property Predictions. For each of the polymerized, equilibrated neat PLA/PETG and PLA/PETG−glass/iron nanocomposite replicates, the elastic modulus, Poisson's ratio, shear modulus, and bulk modulus were predicted according to the standard MD methodology.[43,44,46] The number of samples used to compute the averages of density (ρ) and bulk modulus (K) is 10. The number of samples used to compute the averages of elastic modulus (E), shear modulus (G), and Poisson's ratio (ν) is 30. In the standard MD methodology, each MD model is strained uniaxially and in shear in the three Cartesian axes and planes, respectively. In this work, the old in-house R tool used to analyze the stress−strain curves was replaced with a new in-house Python tool using the "piecewise-regression" Python package.[83] Example

plots for elastic modulus, Poisson's ratio, and shear modulus can be seen in the Supporting Information as Figures S3–S5, respectively.

Micromechanics. NASMAT[68,69] can predict mechanical properties of PLA/PETG–glass/iron composites across a range of vol % glass/iron by using only the neat and highly loaded MD predictions as input; this approach has been used successfully in the past.[55,59] In NASMAT, the generalized method of cells was used to calculate the homogenized mechanical properties of a 2 × 2 × 2 three-dimensional triply periodic repeating unit cell containing the properties of both neat and nanocomposite MD systems. The mechanical properties of the neat PLA/PETG MD systems were assigned to seven of the eight cells, while the nanocomposite properties were assigned to the eighth cubic cell. Due to periodicity, this setup simulates NPs of PLA/PETG–glass/iron embedded in neat PLA/PETG. In the NASMAT input decks, the elastic modulus and Poisson's ratio of neat and nanocomposite were drawn randomly from a normal distribution of the averaged neat and nanocomposite MD properties. Mechanical isotropy of both neat and nanocomposite was enforced via $G = \frac{E}{2(1 + \nu)}$.

The neat polymer can reasonably be assumed to be isotropic. The nanocomposites represent glass/iron NPs spread throughout polymer matrix; this type of material is often isotropic; thus, isotropy of the nanocomposites is enforced here. Due to the random drawing of elastic moduli, each volume percent of glass/iron was run 500 times, and the results were averaged.

■ EXPERIMENTAL METHODS

PLA was sourced from MatterHackers (Translucent Clear ProSeries) as a filament with a diameter of 1.75 mm and a density of 1.25 g cm⁻³. PETG was sourced from MatterHackers (ProSeries) as a filament with a diameter of 1.75 mm and a density of 1.335 g cm⁻³. The filament was then pelletized for extrusion. CIP (CM GRADE) from BASF had a density of 7.9 g cm⁻³ and an average particle size of 10 μm. Hollow G-800 Ceramic Microspheres (MS) were purchased from Zeeospheres Ceramic, LLC, and had a density of 2.2 g cm⁻³ and an average particle size of 14 μm.

Extrusion was performed by using a Thermo Fisher Process 11 twin-screw extruder. A calibration curve was made by collecting three samples from both the additive and polymer feeders for one min each to determine linearity. We point out the reason behind the 3.94 and 7.77 vol % of the MS/CIP loadings in PLA and PETG. The initial target blending ratios for polymer and fillers were 2.5 and 5.0% by volume. When initial batching was performed using PLA and MS, the true density of the MS as reported in the product literature ($\rho = 2.2$ g cm⁻³) was used for calculations. However, the reported true density of MS did not take into account the hollowness. As such, the hollow MS actually took up a larger bulk volume of the polymer blend than originally intended. The bulk density of the MS was experimentally determined to be 1.375 g cm⁻³. Subsequently, the volume percentages of fillers were recalculated to be 3.94 and 7.77%. These new volume percentages were then held constant for all other blends. In terms of mass, the loadings are for PLA/MS, 4.35 and 8.54%; for PLA/CIP, 20.63 and 34.81%; and for PETG/CIP, 20.25 and 34.27%. Using an excel spreadsheet, the polymer and additive feed rates with the least deviation were selected to yield the desired composite wt %. Based on the melting point, the temperature profile chosen for this material was 200 °C for

zones 2–8 and 190 °C for the die, where zone one is chilled. This profile was chosen to ensure proper flow and low torque on the extruder. Once a steady state flow was achieved, dog bones and disks (2 mm thickness × 25 mm diameter) were injection molded using a Thermo Scientific HAAKE MiniJet Pro Injection Molding system at 200 °C and 400 psi. It is important to note that due to project limitations, there was only enough MS available to manufacture the PLA/MS composites.

Density measurements were recorded using a Sartorius balance and density measuring kit according to ASTM D792. Tensile testing was performed using an Instron ElectroPuls E3000 instrument equipped with a 5 kN load cell. Samples were tested using a constant tensile displacement of 2 mm/min according to ASTM D-638.

■ RESULTS AND DISCUSSION

Experimental Tensile Testing. The mechanical response of the PLA/PETG–MS/CIP composites is shown in Figures 6–8, and the elastic/specific-elastic moduli are shown in Table
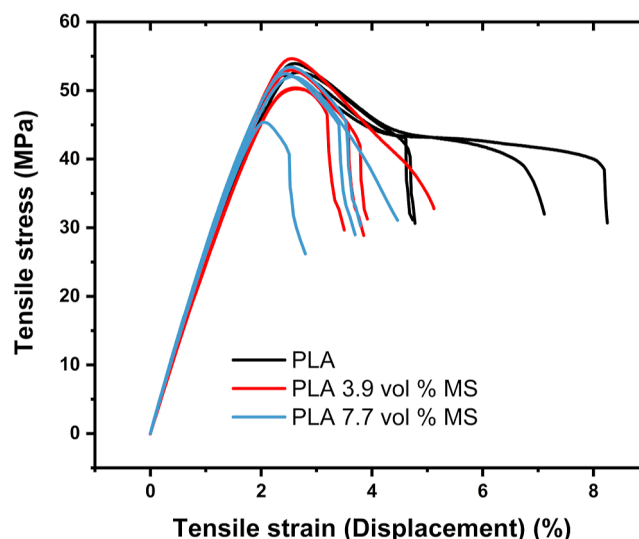

Figure 6. Experimental mechanical response of PLA with glass MS. Four samples were manufactured for each loading (neat, 3.9 vol %, 7.7 vol %).

2. In all of the PLA composites, the overall tensile strain behavior decreased. The 7.77 vol % CIP PETG–CIP samples had some observable variance in the strain to break behavior. The neat PLA samples produced elastic modulus values of 2.65 ± 0.04 GPa. The addition of the MS produced modulus values of 2.67 ± 0.10 and 2.81 ± 0.04 GPa for 3.94 vol % (0.59% increase) and 7.77 vol % (6.08% increase), respectively. The PLA–CIP composites showed larger average elastic moduli but also had more variance in performance. The 3.94 vol % CIP had an elastic modulus value of 2.81 GPa, and the 7.77 vol % CIP exhibited a value of 3.31 GPa which equates to 6.02 and 24.88% increases compared to the neat PLA. The Young's modulus of PETG was calculated to be 2.12 ± 0.08 GPa. With the addition of CIP into PETG, the Young's moduli values increased to 2.45 and 2.69 GPa for 3.94 and 7.7 vol % CIP, respectively. This corresponded to 15.68 and 27.08% increases compared to the neat PETG. The specific elastic moduli of the filled polymers are all roughly equal or smaller than those of the neat polymer.
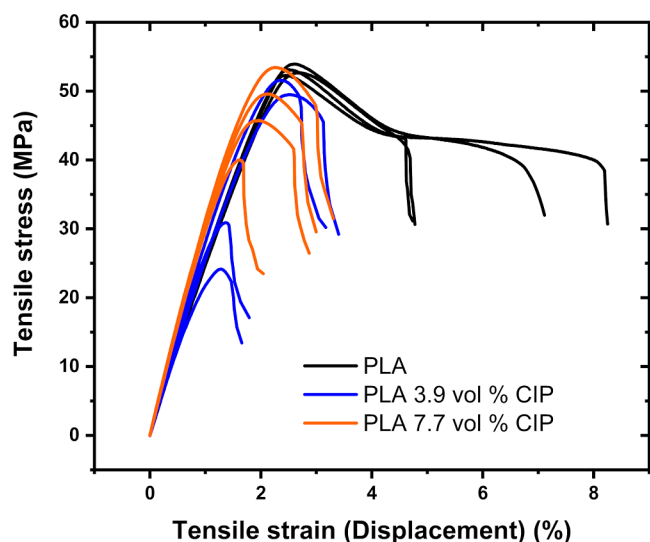
Figure 7. Experimental mechanical response of PLA with CIP. Four samples were manufactured for each loading (neat, 3.9 vol %, 7.7 vol %).
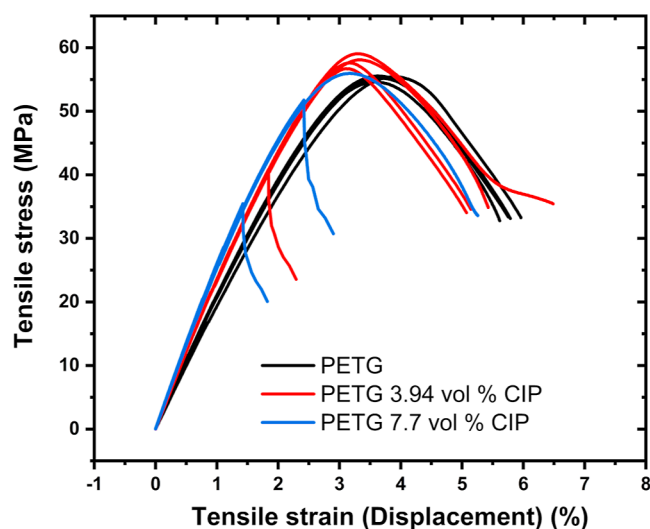

Figure 8. Experimental mechanical response of PETG with CIP. The number of manufactured samples per loading is as follows: four samples of neat PETG, five samples of PETG at 3.94 vol %, and three samples of PETG at 7.77 vol %.

Table 2. Elastic Modulus (E) and Specific Elastic Modulus (E/ρ) of the Experimental PLA/PETG−MS/CIP Composites

polymer	filler	vol %	E (GPa)	E/ρ (GPa/g cm^{-3})
PLA			2.65 ± 0.04	2.13 ± 0.03
PLA	MS	3.94	2.67 ± 0.10	2.11 ± 0.08
PLA	MS	7.77	2.81 ± 0.04	2.17 ± 0.03
PLA	CIP	3.94	2.81 ± 0.13	1.82 ± 0.08
PLA	CIP	7.77	3.31 ± 0.05	1.75 ± 0.03
PETG			2.12 ± 0.08	1.59 ± 0.06
PETG	CIP	3.94	2.45 ± 0.02	1.58 ± 0.01
PETG	CIP	7.77	2.69 ± 0.04	1.48 ± 0.02

Interaction Energy. The interaction energy between the polymer matrix and reinforcement is one metric for determining the strength of the interface. If the interface is

strong, then load will be transferred from the matrix to the reinforcement. Generally, the reinforcement can take a significantly larger amount of load than that of the matrix. If loading is transferred from the matrix to reinforcement, the overall composites can survive in more stressful conditions. In this study, we used glass and iron NPs of different sizes, and therefore the interaction energies of the nanocomposites cannot be compared directly. By normalizing the interaction energies by the number of atoms in each reinforcement, we can compare the PLA/PETG nanocomposites.

Table 3 shows the interaction energies of the PLA/PETG glass/iron nanocomposites divided by the number of atoms in

Table 3. Interaction Energies on a Per-atom-reinforcement Basis of the PLA−Glass/Iron and PETG−Glass/Iron Nanocomposites in kcal/mol

polymer	filler	interaction energy
PLA	iron	−2.20 ± 0.02
PLA	glass	−0.63 ± 0.03
PETG	iron	−2.00 ± 0.02
PETG	glass	−0.50 ± 0.02

the NP. With interaction energies, the more negative the value, the more strongly attracted together the matrix and reinforcement are. The polymer matrices are both more strongly attracted to iron than the glass. It is possible to break down the interaction energy of the overall polymer into the interaction energy of each atom type with the NP. Upon examination of the average interaction energy breakdown (on a per-filler-atom basis) for each PLA/glass and PLA/iron (Figure S6), the PLA oxygen atoms have a positive interaction energy (repulsion) with the glass NP, while they have a negative interaction energy (attraction) with the iron NP. The oxygen atoms of both PLA and glass have a negative charge, thus repulsion is to be expected. The PETG/glass behaves similarly, with the polymer oxygen atoms having a repulsive energy with the glass while they have an attractive energy with the iron. We believe that if the iron NP had an oxide surface, then the attraction of the polymer to the iron NP would be of a similar strength as the glass NP. The glass and iron NPs are slightly more attracted to PLA than PETG. Both PLA and PETG are attracted to the glass NP, largely due to the alcohol group's hydrogen atoms. However, the molecular structure of PLA has two alcohol groups, while PETG has only one (see Figures 1 and 2). Thus, PLA is more attracted to the glass NP than PETG due to the extra alcohol group. PLA has a greater attraction to the iron NP than PETG because the oxygen and carbon atoms in PLA's alcohol and ketone groups and carbon backbone simply interact significantly more strongly with the iron NP than these groups do in PETG (see Figure S6).

Mechanical Properties. *Molecular Dynamics.* The elastic moduli and densities of the neat PLA/PETG and glass/iron nanocomposites are shown in Table 4. Table 5 shows the average mechanical property predictions normalized by the neat PLA/PETG values to more easily show the relative increase/decrease in elastic moduli and density. Elastic modulus (E) increased significantly from neat for PLA/glass, PLA/iron, and PETG/iron. The glass NP did not reinforce the PETG matrix as much as it reinforced the PLA matrix; the degree of reinforcement is less than 20% across the elastic modulus, bulk modulus (K), and shear modulus (G). Poisson's ratio (ν) does not change significantly for the PLA/PETG−

Table 4. Mechanical Property Predictions of MD Systems[a]

polymer	filler (vol %)	ρ (g cm^{-3})	K (GPa)	E (GPa)	ν	G (GPa)
PLA		1.246 ± 0.010	4.17 ± 0.30	2.42 ± 0.32	0.35 ± 0.06	0.89 ± 0.15
	glass (22)	1.522 ± 0.003	7.38 ± 0.28	4.26 ± 0.64	0.34 ± 0.07	1.44 ± 0.26
	iron (17)	2.442 ± 0.007	9.04 ± 0.37	5.17 ± 1.04	0.33 ± 0.08	1.72 ± 0.37
PETG		1.239 ± 0.001	6.11 ± 0.15	1.98 ± 0.28	0.41 ± 0.06	0.66 ± 0.12
	glass (22)	1.441 ± 0.005	6.46 ± 0.26	2.37 ± 0.43	0.41 ± 0.10	0.76 ± 0.17
	iron (16)	2.351 ± 0.006	8.07 ± 0.34	3.42 ± 0.65	0.36 ± 0.09	0.90 ± 0.20

[a]Density is ρ, bulk modulus is K, elastic modulus is E, Poisson's ratio is ν, and shear modulus is G.

Table 5. Normalized Average Mechanical Property Predictions of MD Systems[a]

polymer	filler	ρ_N	K_N	E_N	ν_N	G_N
PLA		1.00	1.00	1.00	1.00	1.00
	glass	1.22	1.77	1.76	0.97	1.61
	iron	1.96	2.17	2.13	0.93	1.93
PETG		1.00	1.00	1.00	1.00	1.00
	glass	1.16	1.06	1.20	1.00	1.16
	iron	1.90	1.32	1.73	0.88	1.38

[a]Density is ρ_N, bulk modulus is K_N, elastic modulus is E_N, Poisson's ratio is ν_N, and shear modulus is G_N.

Table 6. Computed Specific Moduli and Specific Poisson's Ratio Obtained by Dividing with the Corresponding Density of MD Systems[a]

polymer	filler	K/ρ	E/ρ	ν/ρ	G/ρ
PLA		3.35	1.94	0.28	0.72
	glass	4.85	2.80	0.22	0.94
	iron	3.70	2.12	0.13	0.70
PETG		4.94	1.60	0.33	0.53
	glass	4.48	1.64	0.28	0.53
	iron	3.43	1.45	0.15	0.38

[a]Specific moduli are in units of GPa/g cm^{-3}, and specific Poisson's ratio is in units of 1/g cm^{-3}.

glass nanocomposites but does for the PLA/PETG−iron nanocomposites. The PLA/PETG−iron nanocomposites have a greater interaction energy than the PLA/PETG−glass nanocomposites; also, it is possible that the stronger interface causes the polymers to shrink less in the transverse direction when stretched in the axial direction. Moreover, the relative rigidity of the iron versus the glass might also be affecting the Poisson's ratio. For both PLA and PETG, the iron NP provides a greater degree of reinforcement than the glass NP because iron has greater elastic moduli than glass. The degree of reinforcement of both glass and iron is greater for PLA than PETG. Computationally, this could be due to the slightly greater attraction between the glass/iron NP and the PLA matrix. In the experimental samples, the iron reinforcement provides greater reinforcement for PETG than PLA. It is known that CIP has a metal oxide layer as well as a SiO_2 layer for enhanced magnetization.[84] It is possible that in the experimental samples, the metal oxide and SiO_2 layers interact more strongly with the PETG than the PLA.

A significant advantage of polymer composites is their general potential for excellent mechanical properties while being lighter than metal alloys. One area where polymer composites have been used to great success is the aerospace industry.[85] By replacing metal alloys with lighter-weight yet strong and stiff polymer composites, aerospace companies have enabled greater fuel efficiency in their aircraft. Thus, with a high density filler such as iron, it is important to evaluate the specific elastic moduli (elastic moduli divided by the density). Table 6 shows that the specific elastic moduli of the glass nanocomposites are greater than those of the iron nano-composites. The PLA/glass and PLA/iron nanocomposites exhibit a 44 and 9% improvement in specific elastic modulus, respectively. However, the PETG/glass nanocomposite exhibits a 2.5% improvement in specific elastic modulus, while the PETG/iron exhibits a 9% decrease. Therefore, if density is a concern, we do not recommend using PETG reinforced with iron NPs. If density is not a concern, then Table 4 shows significant increases in the elastic moduli with the iron-reinforced composites. The MD-specific moduli trends

contrast with the experimental results. The experimental samples are loaded significantly less than the MD models, and it is probable that, with these glass and iron fillers, significant improvement in specific elastic moduli will only occur at relatively high loadings.

PLA has been researched using MD simulations several times.[86−93] Studies range from predicting the shape-memory behavior of PLA[86,91,92] to investigating how chain scission and solvation affect the biodegradation of PLA[90] to creating coarse-grained force fields for PLA[88,89] to exploring the interface of PLA with attapulgite[87] to predicting the thermo-mechanical properties of PLA.[93] Three of these computational studies reported mechanical properties.[89,90,93] Two of them[89,90] only reported elastic modulus, while the third[93] reported elastic modulus, Poisson's ratio, and shear modulus. The coarse-grained elastic modulus predictions of Glagolev and Vasilevskaya[89] are reported in hundreds of MPa, which is significantly lower than experiment; the reported density is also significantly lower than experiment, which can significantly affect thermo-mechanical properties. Alex et al.[90] reported an elastic modulus of 4 GPa but did not compare it to experiment. They conducted nanoDMA analysis of neat PLA and found that the storage modulus varied from 1 to 3 GPa. In some cases, it is reasonable to assume that the storage modulus is approximately equal to the elastic modulus. However, their MD elastic modulus prediction does not compare well with their experimental data.[90] Alex et al.[90] used a PLA-specific force field called PLAFF3[94] that was, to our knowledge, never validated for mechanical property predictions, thus explaining this discrepancy. The third study by Xiang et al.[93] predicted elastic modulus, Poisson's ratio, and shear modulus of neat PLA using the COMPASS force field[95] which has been validated numerous times for polymers.[96] Our neat PLA elastic modulus (2.42 ± 0.32 GPa) compares fairly well with their value of 1.83 GPa. Additionally, our neat PLA shear modulus (0.89 ± 0.15 GPa) compares well with their value of 0.82 GPa. Although our neat PLA Poisson's ratio (0.35 ± 0.06) does not compare well with their predicted value of 0.12,[93] it shows
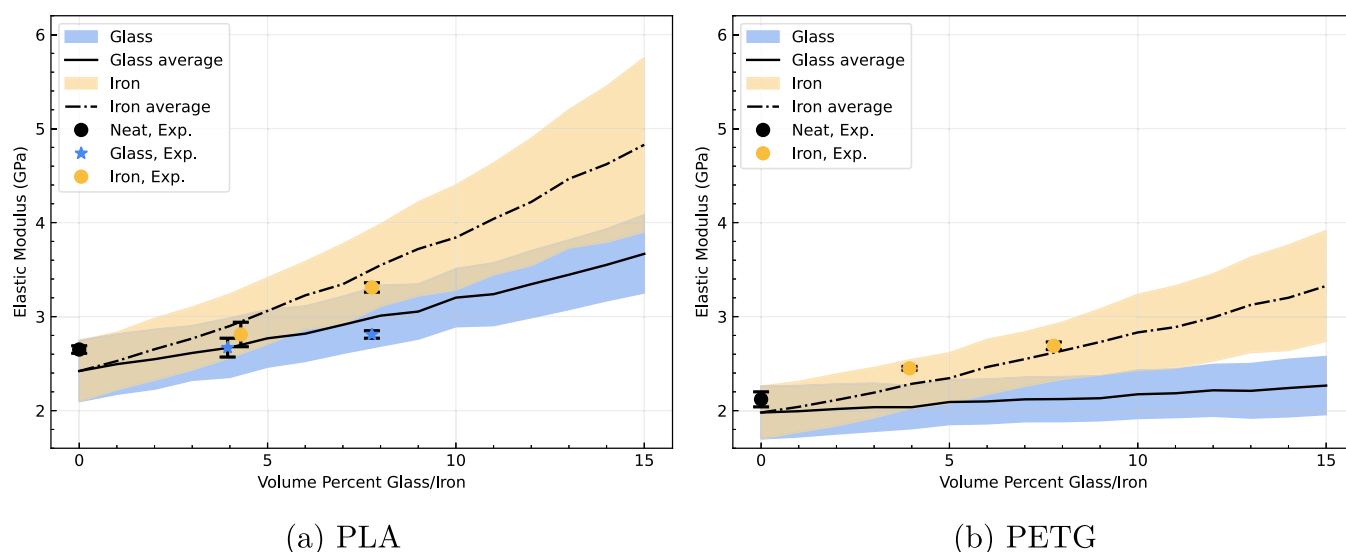
(a) PLA

(b) PETG

Figure 9. Elastic modulus NASMAT predictions for PLA−glass/iron (a) and PETG−glass/iron (b) nanocomposites. Please note that the 3.94 vol % PLA−iron experimental data point was shifted to the right by 0.35 vol % for clarity. The shaded area (dark tan) between the iron (tan color) and glass (blue color) shows the overlap between the two data sets. The elastic modulus values at 0 vol % are MD predictions. Please see Tables S2−S5 for the NASMAT and MD predictions side-by-side.
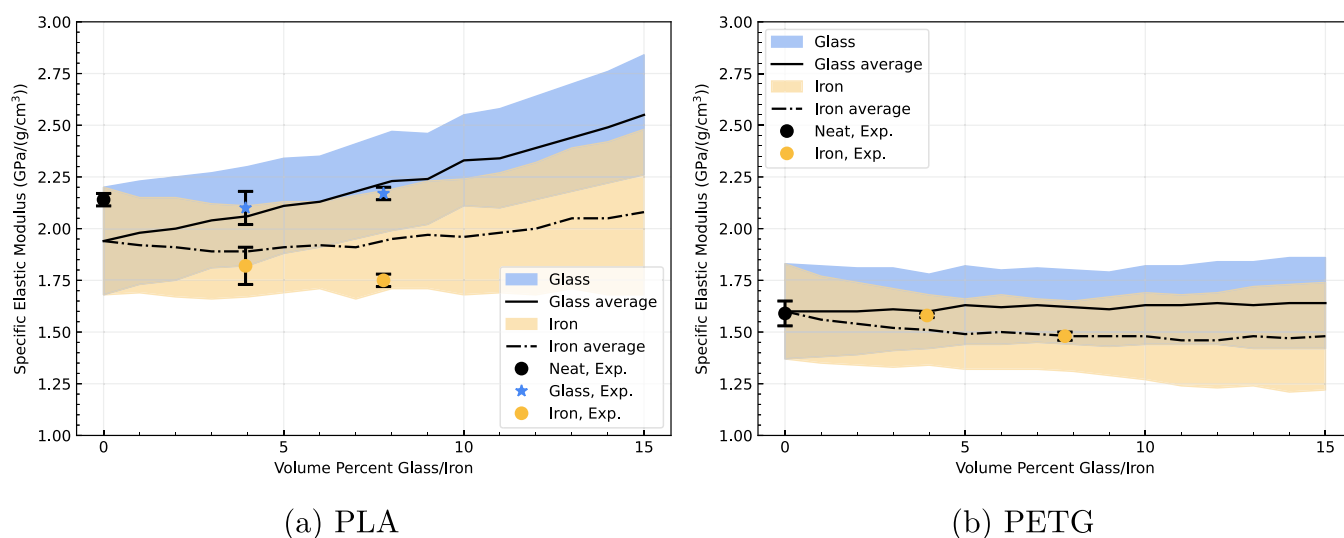

(a) PLA

(b) PETG

Figure 10. Specific elastic modulus NASMAT predictions for PLA−glass/iron (a) and PETG−glass/iron (b) nanocomposites. The shaded area (dark tan) between the iron (tan color) and glass (blue color) shows the overlap between the two data sets. The elastic modulus values at 0 vol % are MD predictions. Please see Tables S2−S5 for the NASMAT and MD predictions side-by-side.

excellent agreement with the experimental Poisson's ratio, which is close to 0.33.[97] We were not able to find any MD simulation studies of PETG in the open literature.

Micromechanics. In this study, our goal was to understand how the mechanical properties of PLA/PETG−glass/iron composites change as the volume percent (vol %) of glass/iron increases from 0 to 20 vol %. MD models with a relatively high loading of glass and iron at 20 vol % in PLA and PETG were created. The vol % was initially 20 vol % but drifted later on in the creation process with a minimum of 16 vol % and a maximum of 22 vol %. MD models with differing vol % filler cannot be directly compared as differences in properties are likely due to the difference in loading. However, it is possible to use a micromechanics approach to predict mechanical properties over a range of loadings using the neat and glass/iron-filled MD predictions as input.[55,59] This enables a

comparison of mechanical properties of previously uncomparable MD models. Additionally, it is no longer required to create multiple MD models per vol % per polymer/filler combination to determine the effect of loading on mechanical properties with this micromechanical dilution scheme. This vastly reduces the time, effort, and computational resources required for such a study. Due to the drift from 20 vol %, the range of study shifted to 0−15 vol % as shown in Figures 9, 10, and S7−S14.

Figure 9 shows the predicted elastic modulus of the PLA−glass/iron and PETG−glass/iron nanocomposites as a function of volume percent glass/iron. PLA is a slightly stiffer polymer than PETG, and thus the PLA−glass/iron predictions start slightly higher. However, the reinforcing effect of the glass/iron NPs is significantly greater for PLA than PETG. For both PLA and PETG, the iron nanocomposites exhibit a higher elastic

modulus than the glass nanocomposites at all loadings, which is expected because iron is significantly stiffer than glass. The PLA predictions steadily increase with increasing vol % glass/iron. PETG/iron behaves similarly, albeit with a much smaller increase, but PETG/glass increases slowly with increasing vol % glass and ends up about 14.5% higher than neat PETG. However, the increase in elastic modulus from neat PETG to 15 vol % glass is small, 0.29 GPa, which gives the appearance that the PETG/glass curve in Figure 9 is flat. Experimental data are included in Figure 9 for validation of the modeling. The predictions match the experimental data well, with all experimental data points being encompassed by the predictions' standard deviation, which limits the extents of the blue and tan-shaded regions. The PLA/iron experimental data matches best, followed by PLA/glass and PETG/iron.

Figure 10 shows the predicted specific elastic modulus of the PLA−glass/iron and PETG−glass/iron nanocomposites as a function of volume percent glass/iron. Figure 10 shows that the specific modulus of PLA/glass steadily increases, while PLA/iron decreases from 0 to 5 vol % and then slowly increases to slightly above the starting value by 15 vol %. The PETG/glass predictions remain nearly constant with increasing vol % glass/iron, while the PETG/iron predictions steadily decrease. The experimental data correlates well with the predictions, with the PLA/glass data matching best, followed by PETG/iron and PLA/iron.

It is important to note that there are several factors that differ between simulation and experiment, such as strain rate, crystallinity, and molecular weight, that should result in a poorer comparison. All polymers exhibit a phenomenon called the strain rate effect, in which the faster a polymer experiences deformation, the stiffer and stronger the polymer will be. In predicting the elastic moduli, the polymer MD models had to be strained significantly faster (due to computational rigor) than the experimental samples, which should result in significantly higher elastic and shear moduli. In semicrystalline polymers, there exist two phases: a softer, more pliable amorphous phase and a stiffer, more brittle crystalline phase. The experimental PLA composites are semicrystalline, whereas the MD models are amorphous, which should result in the MD predictions having lower elastic and shear moduli. The molecular weight of a polymer signifies how long the polymer's chains are on average. A polymer sample with longer chains than another sample will typically exhibit a larger elastic modulus because the longer chains are more entangled with each other and can stretch further before failure. The molecular weight between MD and experiment is likely different, but historically, with MD, molecular weight does not usually affect the comparison of mechanical properties between simulation and experiment. This is due to the periodicity of the MD models, which allows the MD models to behave as bulk systems. In the case of PLA, the strain rate effect and the lack of crystallinity of the MD models likely canceled each other out, with the overall effect being mechanical properties similar to those of the experiment. In the case of PETG matching so well even with the strain rate effect, it is possible that the significantly higher strain rate of the MD simulations does not always result in a clear strain rate effect. The strain rate effect is not always seen with every polymer in every MD force field.

Figures S7−S14 show the NASMAT predictions of Poisson's ratio and the shear modulus of the PLA−glass/iron and PETG−glass/iron nanocomposites. We included these plots in the Supporting Information because we do not have experimental data for Poisson's ratio or shear modulus for any of the studied systems.

CONCLUSIONS

The mechanical response of PLA−glass/iron and PETG−glass/iron nanocomposites at a relatively high loading was predicted using MD simulations with the reactive IFF. The NASMAT was used to predict the mechanical response across the range of 1−15 vol % glass/iron filler by using only the neat and highly loaded MD predictions as input. This approach vastly reduces the time, effort, and computational resources required. Experimental samples incorporating hollow glass MS and CIP into PLA/PETG were manufactured and tested for the elastic modulus. Experimentally, the CIP produced a larger reinforcement in elastic modulus than the MS, with similar increases in elastic modulus between PLA/CIP and PETG/CIP at 7.77 vol % CIP. Computationally, we found that the iron and glass NPs significantly increased the elastic moduli of the PLA matrix, while the PETG matrix exhibited modest increases in elastic moduli. This difference in reinforcement ability may be due to the slightly greater attraction between glass/iron NP and PLA matrix. The micromechanics-based mechanical predictions compare excellently with the experimental values, validating the integrated micromechanical/MD simulation-based approach.

ASSOCIATED CONTENT

ⓢ Supporting Information

The Supporting Information is available free of charge at https://pubs.acs.org/doi/10.1021/acsomega.3c08264.

> In-depth MD methodologies, example mechanical property prediction plots, molecular weight information, interaction energy breakdowns, NASMAT predictions alongside MD predictions, and micromechanics prediction plots for Poisson's ratio and shear modulus (PDF)

AUTHOR INFORMATION

Corresponding Author

Manoj K. Shukla − *Environmental Laboratory, US Army Engineer Research and Development Center, Vicksburg, Mississippi 39180, United States;* ⓘ orcid.org/0000-0002-7560-1172; Email: manoj.k.shukla@usace.army.mil

Authors

William A. Pisani − *Oak Ridge Institute for Science and Education, Oak Ridge, Tennessee 37831, United States; Environmental Laboratory, US Army Engineer Research and Development Center, Vicksburg, Mississippi 39180, United States;* ⓘ orcid.org/0000-0002-5172-862X

Dane N. Wedgeworth − *Geotechnical and Structures Laboratory, US Army Engineer Research and Development Center, Vicksburg, Mississippi 39180, United States*

Jedadiah F. Burroughs − *Geotechnical and Structures Laboratory, US Army Engineer Research and Development Center, Vicksburg, Mississippi 39180, United States*

Travis L. Thornell − *Geotechnical and Structures Laboratory, US Army Engineer Research and Development Center, Vicksburg, Mississippi 39180, United States*

J. Kent Newman − *Geotechnical and Structures Laboratory, US Army Engineer Research and Development Center, Vicksburg, Mississippi 39180, United States*

Complete contact information is available at:
https://pubs.acs.org/10.1021/acsomega.3c08264

Notes
The authors declare no competing financial interest.

■ REFERENCES

(1) Rijckaert, S.; Daelemans, L.; Cardon, L.; Boone, M.; Van Paepegem, W.; De Clerck, K. Continuous Fiber-Reinforced Aramid/PETG 3D-Printed Composites with High Fiber Loading through Fused Filament Fabrication. *Polymers* **2022**, *14*, 298.

(2) Colón Quintana, J. L.; Slattery, L.; Pinkham, J.; Keaton, J.; Lopez-Anido, R. A.; Sharp, K. Effects of Fiber Orientation on the Coefficient of Thermal Expansion of Fiber-Filled Polymer Systems in Large Format Polymer Extrusion-Based Additive Manufacturing. *Materials* **2022**, *15*, 2764.

(3) Szykiedans, K.; Credo, W.; Osiński, D. Selected Mechanical Properties of PETG 3-D Prints. *Procedia Eng.* **2017**, *177*, 455−461.

(4) Soleyman, E.; Aberoumand, M.; Rahmatabadi, D.; Soltanmohammadi, K.; Ghasemi, I.; Baniassadi, M.; Abrinia, K.; Baghani, M. Assessment of controllable shape transformation, potential applications, and tensile shape memory properties of 3D printed PETG. *J. Mater. Res. Technol.* **2022**, *18*, 4201−4215.

(5) Santana, L.; Alves, J. L.; Sabino Netto, A. d. C.; Merlini, C. Estudo comparativo entre PETG e PLA para Impressão 3D através de caracterização térmica, química e mecânica. *Rev. Mater.* **2018**, *23*, No. e12267.

(6) Valvez, S.; Silva, A. P.; Reis, P. N. Optimization of Printing Parameters to Maximize the Mechanical Properties of 3D-Printed PETG-Based Parts. *Polymers* **2022**, *14*, 2564.

(7) Algarni, M.; Ghazali, S. Comparative study of the sensitivity of pla, abs, peek, and petg's mechanical properties to fdm printing process parameters. *Crystals* **2021**, *11*, 995.

(8) Moreno Nieto, D.; Alonso-García, M.; Pardo-Vicente, M. A.; Rodríguez-Parada, L. Product design by additive manufacturing for water environments: Study of degradation and absorption behavior of pla and petg. *Polymers* **2021**, *13*, 1036.

(9) Wojnowski, W.; Marć, M.; Kalinowska, K.; Kosmela, P.; Zabiegała, B. Emission Profiles of Volatiles during 3D Printing with ABS, ASA, Nylon, and PETG Polymer Filaments. *Molecules* **2022**, *27*, 3814−3819.

(10) Vidakis, N.; Petousis, M.; Velidakis, E.; Liebscher, M.; Mechtcherine, V.; Tzounis, L. On the strain rate sensitivity of fused filament fabrication (Fff) processed pla, abs, petg, pa6, and pp thermoplastic polymers. *Polymers* **2020**, *12*, 2924−3015.

(11) Talataisong, W.; Ismaeel, R.; Marques, T. H.; Abokhamis Mousavi, S.; Beresna, M.; Gouveia, M. A.; Sandoghchi, S. R.; Lee, T.; Cordeiro, C. M.; Brambilla, G. Mid-IR Hollow-core microstructured fiber drawn from a 3D printed PETG preform. *Sci. Rep.* **2018**, *8*, 8113−8118.

(12) Barrios, J. M.; Romero, P. E. Improvement of surface roughness and hydrophobicity in PETG parts manufactured via fused deposition modeling (FDM): An application in 3D printed self-cleaning parts. *Materials* **2019**, *12*, 2499.

(13) Shilov, S. Y.; Rozhkova, Y. A.; Markova, L. N.; Tashkinov, M. A.; Vindokurov, I. V.; Silberschmidt, V. V. Biocompatibility of 3D-Printed PLA, PEEK and PETG: Adhesion of Bone Marrow and Peritoneal Lavage Cells. *Polymers* **2022**, *14*, 3958.

(14) Valvez, S.; Silva, A. P.; Reis, P. N. Compressive Behaviour of 3D-Printed PETG Composites. *Aerospace* **2022**, *9*, 124.

(15) Kováčová, M.; Kozakovičová, J.; Procházka, M.; Janigová, I.; Vysopal, M.; Černičková, I.; Krajčovič, J.; Špitalský, Z. Novel hybrid PETG composites for 3D printing. *Appl. Sci.* **2020**, *10*, 3062.

(16) Hsueh, M. H.; Lai, C. J.; Wang, S. H.; Zeng, Y. S.; Hsieh, C. H.; Pan, C. Y.; Huang, W. C. Effect of printing parameters on the thermal and mechanical properties of 3d-printed pla and petg, using fused deposition modeling. *Polymers* **2021**, *13*, 1758.

(17) Yang, S. l.; Wu, Z. H.; Yang, W.; Yang, M. B. Thermal and mechanical properties of chemical crosslinked polylactide (PLA). *Polym. Test.* **2008**, *27*, 957−963.

(18) Grasso, M.; Azzouz, L.; Ruiz-Hincapie, P.; Zarrelli, M.; Ren, G. Effect of temperature on the mechanical properties of 3D-printed PLA tensile specimens. *Rapid Prototyp. J.* **2018**, *24*, 1337−1346.

(19) Coppola, B.; Cappetti, N.; Maio, L. D.; Scarfato, P.; Incarnato, L. 3D printing of PLA/clay nanocomposites: Influence of printing temperature on printed samples properties. *Materials* **2018**, *11*, 1947.

(20) Greco, A.; Ferrari, F. Thermal behavior of PLA plasticized by commercial and cardanol-derived plasticizers and the effect on the mechanical properties. *J. Therm. Anal. Calorim.* **2021**, *146*, 131−141.

(21) Ghasemi, S.; Behrooz, R.; Ghasemi, I.; Yassar, R. S.; Long, F. Development of nanocellulose-reinforced PLA nanocomposite by using maleated PLA (PLA-g-MA). *J. Thermoplast. Compos. Mater.* **2018**, *31*, 1090−1101.

(22) Sztorch, B.; Brząkalski, D.; Pakuła, D.; Frydrych, M.; Špitalský, Z.; Przekop, R. E. Natural and Synthetic Polymer Fillers for Applications in 3D Printing—FDM Technology Area. *Solids* **2022**, *3*, 508−548.

(23) Guo, B.; Xu, Z.; Luo, X.; Bai, J. A detailed evaluation of surface, thermal, and flammable properties of polyamide 12/glass beads composites fabricated by multi jet fusion. *Virtual Phys. Prototyp.* **2021**, *16*, S39−S52.

(24) Rath, U.; Pandey, P. M. Investigations into the microwave shielding behavior of oriented Polycaprolactone/Carbonyl iron particles composites fabricated using magnetic field assisted extrusion 3D printing. *Proc. Inst. Mech. Eng., Part C* **2021**, *235*, 2768−2781.

(25) Pei, Z.; Xu, Y.; Wei, F.; Liu, T.; Su, D. Electromagnetic property of a novel gradient honeycomb composite fabricated by 3D forming. *J. Magn. Magn. Mater.* **2020**, *493*, 165742.

(26) Wang, F.; Zhou, Q.; Zhang, Z.; Gu, Y.; Zhang, J.; Jiang, K. Microwave Absorption Properties of Carbon Black-Carbonyl Iron/Polylactic Acid Composite Filament for Fused Deposition Modeling. *Materials* **2022**, *15*, 5455.

(27) Singh, J.; Kaur, T.; Singh, N.; Pandey, P. M. Biological and mechanical characterization of biodegradable carbonyl iron powder/polycaprolactone composite material fabricated using three-dimensional printing for cardiovascular stent application. *Proc. Inst. Mech. Eng., Part H* **2020**, *234*, 975−987.

(28) Chawla, K. K. *Composite Materials*; Springer New York: New York, NY, 2012.

(29) Daniel, I. M.; Ishai, O. *Engineering Mechanics of Composite Materials; Engineering Mechanics of Composite Materials*; Oxford University Press, 1994.

(30) Narkis, M.; Nicolais, L. Stress−strain behavior of SAN/glass bead composites above the glass transition temperature. *J. Appl. Polym. Sci.* **1971**, *15*, 469−476.

(31) Leidner, J.; Woodhams, R. T. The strength of polymeric composites containing spherical fillers. *J. Appl. Polym. Sci.* **1974**, *18*, 1639−1654.

(32) Kang, B.-h.; Lu, X.; Qu, J.-p.; Yuan, T. Synergistic effect of hollow glass beads and intumescent flame retardant on improving the fire safety of biodegradable poly (lactic acid). *Polym. Degrad. Stab.* **2019**, *164*, 167−176.

(33) Yoon, C. K.; Park, B. K.; Lee, W. I. Characteristics of micro-glass bead/PLA porous composite prepared by electrospinning. *Adv. Compos. Mater.* **2018**, *27*, 183−193.

(34) Yao, R.; Yao, Z.; Zhou, J.; Zhou, C. Microcosmic morphology and properties of hollow glass beads-reinforced polylactic acid-based foam composites. *Polym. Compos.* **2016**, *37*, 692−699.

(35) Yao, R.; Yao, Z.; Zhou, J.; Liu, P. Mechanical and acoustical properties of polylactic acid based multilayer-structured foam biocomposites. *J. Reinf. Plast. Compos.* **2016**, *35*, 785−795.

(36) Rodriguez Lorenzana, F. A. Thermal Characterization of ABS/ Carbon Fiber, ABS/ Glass Fiber and PETG/Glass Fiber Reinforced Composites Used in Large Area Additive Manufacturing. Ph.D. thesis, 2019.

(37) Fang, F. F.; Liu, Y. D.; Choi, H. J. Fabrication of carbonyl iron embedded polycarbonate composite particles and magnetorheological characterization. *IEEE Trans. Magn.* **2009**, *45*, 2507−2510.

(38) Arias, J. L.; Gallardo, V.; Linares-Molinero, F.; Delgado, A. V. Preparation and characterization of carbonyl iron/poly-(butylcyanoacrylate) core/shell nanoparticles. *J. Colloid Interface Sci.* **2006**, *299*, 599−607.

(39) Dosoudil, R.; Ušáková, M. High-frequency absorbing perform-ances of carbonyl iron/MnZn Ferrite/PVC polymer composites. *Acta Phys. Pol., A* **2017**, *131*, 687−689.

(40) Wang, H.; Zhu, D.; Zhou, W.; Luo, F. Microwave electro-magnetic properties of polyimide/carbonyl iron composites. *J. Polym. Res.* **2014**, *21*, 478.

(41) Pei, Z.; Su, D.; Dai, F.; Liao, Y.; Xu, Y. Absorbing and Shielding Properties of a Hybrid Patterned Composite Containing CIPs and Carbon Fiber. *J. Electron. Mater.* **2018**, *47*, 6591−6599.

(42) Charles, A. D.; Rider, A. N.; Brown, S. A.; Wang, C. H. Improving the actuation performance of magneto-polymer composites by silane functionalisation of carbonyl-iron particles. *Composites, Part B* **2020**, *196*, 108091.

(43) Pisani, W. A.; Wedgeworth, D. N.; Roth, M. R.; Newman, J. K.; Shukla, M. K. Computational Prediction of Mechanical Properties of PA6−Graphene/Carbon Nanotube Nanocomposites. *J. Phys. Chem. C* **2021**, *125*, 15569−15578.

(44) Pisani, W. A.; Newman, J. K.; Shukla, M. K. Multiscale Modeling of Polyamide 6 Using Molecular Dynamics and Micro-mechanics. *Ind. Eng. Chem. Res.* **2021**, *60*, 13604−13613.

(45) Hadden, C. M.; Jensen, B. D.; Bandyopadhyay, a.; Odegard, G. M.; Koo, a.; Liang, R. Molecular modeling of EPON-862/graphite composites: Interfacial characteristics for multiple crosslink densities. *Compos. Sci. Technol.* **2013**, *76*, 92−99.

(46) Pisani, W. A.; Radue, M. S.; Chinkanjanarot, S.; Bednarcyk, B. A.; Pineda, E. J.; Waters, K.; Pandey, R.; King, J. A.; Odegard, G. M. Multiscale Modeling of PEEK using Reactive Molecular Dynamics Modeling and Micromechanics. *Polymer* **2019**, *163*, 96−105.

(47) Radue, M. S.; Jensen, B. D.; Gowtham, S.; Klimek-McDonald, D. R.; King, J. A.; Odegard, G. M. Comparing the Mechanical Response of Di-Tri-and Tetra-Functional Resin Epoxies with Reactive Molecular Dynamics. *J. Polym. Sci., Part B: Polym. Phys.* **2018**, *56*, 255−264.

(48) Bandyopadhyay, A.; Valavala, P. K.; Clancy, T. C.; Wise, K. E.; Odegard, G. M. Molecular modeling of crosslinked epoxy polymers: The effect of crosslink density on thermomechanical properties. *Polymer* **2011**, *52*, 2445−2452.

(49) Patil, S. U.; Radue, M. S.; Pisani, W. A.; Deshpande, P.; Xu, H.; Al Mahmud, H.; Dumitrică, T.; Odegard, G. M. Interfacial characteristics between flattened CNT stacks and polyimides: A molecular dynamics study. *Comput. Mater. Sci.* **2020**, *185*, 109970.

(50) Pisani, W. A.; Radue, M. S.; Patil, S. U.; Odegard, G. M. Interfacial modeling of flattened CNT composites with cyanate ester and PEEK polymers. *Composites, Part B* **2021**, *211*, 108672.

(51) Odegard, G. M.; Jensen, B. D.; Gowtham, S.; Wu, J.; He, J.; Zhang, Z. Predicting Mechanical Response of Crosslinked Epoxy using ReaxFF. *Chem. Phys. Lett.* **2014**, *591*, 175−178.

(52) Gaikwad, P. S.; Kowalik, M.; van Duin, A.; Odegard, G. M. Computational study of effect of radiation induced crosslinking on the properties of flattened carbon nanotubes. *RSC Adv.* **2022**, *12*, 28945−28953.

(53) Tomasi, J.; Pisani, W. A.; Chinkanjanarot, S.; Krieg, A. S.; Jaszczak, D.; Pineda, E. J.; Bednarcyk, B. A.; Miller, S.; King, J. A.; Miskioglu, I.; et al. *Modeling-Driven Damage Tolerant Design of Graphene Nanoplatelet/Carbon Fiber/Epoxy Hybrid Composite Panels for Full-Scale Aerospace Structures*; AIAA Scitech 2019 Forum: Reston, VA, 2019.

(54) Gaikwad, P. S.; Krieg, A. S.; Deshpande, P. P.; Patil, S. U.; King, J. A.; Maiaru, M.; Odegard, G. M. Understanding the Origin of the Low Cure Shrinkage of Polybenzoxazine Resin by Computational Simulation. *ACS Appl. Polym. Mater.* **2021**, *3*, 6407−6415.

(55) Al Mahmud, H.; Radue, M. S.; Chinkanjanarot, S.; Pisani, W. A.; Gowtham, S.; Odegard, G. M. Multiscale modeling of carbon fiber- graphene nanoplatelet-epoxy hybrid composites using a reactive force field. *Composites, Part B* **2019**, *172*, 628−635.

(56) Deshpande, P. P.; Radue, M. S.; Gaikwad, P.; Bamane, S.; Patil, S. U.; Pisani, W. A.; Odegard, G. M. Prediction of the Interfacial Properties of High-Performance Polymers and Flattened CNT-Reinforced Composites Using Molecular Dynamics. *Langmuir* **2021**, *37*, 11526−11534.

(57) Hadden, C.; Klimek-McDonald, D.; Pineda, E.; King, J.; Reichanadter, A.; Miskioglu, I.; Gowtham, S.; Odegard, G. Mechanical Properties of Graphene Nanoplatelet/Carbon Fiber/ Epoxy Hybrid Composites: Multiscale Modeling and Experiments. *Carbon N. Y.* **2015**, *95*, 100−112.

(58) Sachdeva, G.; Patil, S. U.; Bamane, S. S.; Deshpande, P. P.; Pisani, W. A.; Odegard, G. M.; Pandey, R. Mechanical response of polymer/BN composites investigated by molecular dynamics method. *J. Mater. Res.* **2022**, *37*, 4533−4543.

(59) Al Mahmud, H.; Radue, M. S.; Chinkanjanarot, S.; Odegard, G. M. Multiscale Modeling of Epoxy-Based Nanocomposites Reinforced with Functionalized and Non-Functionalized Graphene Nano-platelets. *Polymers* **2021**, *13*, 1958.

(60) Klimek-McDonald, D. R.; King, J. A.; Miskioglu, I.; Pineda, E. J.; Odegard, G. M. Determination and Modeling of Mechanical Properties for Graphene Nanoplatelet/Epoxy Composites. *Polym. Compos.* **2016**, *39*, 1845−1851.

(61) Patil, S. U.; Shah, S. P.; Olaya, M.; Deshpande, P. P.; Maiaru, M.; Odegard, G. M. Reactive Molecular Dynamics Simulation of Epoxy for the Full Cross-Linking Process. *ACS Appl. Polym. Mater.* **2021**, *3*, 5788−5797.

(62) Chinkanjanarot, S.; Radue, M. S.; Gowtham, S.; Tomasi, J. M.; Klimek-McDonald, D. R.; King, J. A.; Odegard, G. M. Multiscale thermal modeling of cured cycloaliphatic epoxy/carbon fiber composites. *J. Appl. Polym. Sci.* **2018**, *135*, 46371.

(63) Odegard, G. M.; Patil, S. U.; Gaikwad, P. S.; Deshpande, P.; Krieg, A. S.; Shah, S. P.; Reyes, A.; Dickens, T.; King, J. A.; Maiaru, M. Accurate predictions of thermoset resin glass transition temperatures from all-atom molecular dynamics simulation. *Soft Matter* **2022**, *18*, 7550−7558.

(64) Heinz, H.; Lin, T.-J.; Kishore Mishra, R.; Emami, F. S. Thermodynamically Consistent Force Fields for the Assembly of Inorganic, Organic, and Biological Nanostructures: The INTERFACE Force Field. *Langmuir* **2013**, *29*, 1754−1765.

(65) Dharmawardhana, C. C.; Kanhaiya, K.; Lin, T.-J.; Garley, A.; Knecht, M. R.; Zhou, J.; Miao, J.; Heinz, H. Reliable Computational Design of Biological-Inorganic Materials to the Large Nanometer Scale using Interface-FF. *Mol. Simul.* **2017**, *43*, 1394−1405.

(66) Winetrout, J. J.; Kanhaiya, K.; Sachdeva, G.; Pandey, R.; Damirchi, B.; van Duin, A.; Odegard, G.; Heinz, H. Implementing

(67) Bamane, S. S.; Gaikwad, P. S.; Radue, M. S.; Gowtham, S.; Odegard, G. M. Wetting Simulations of High-Performance Polymer Resins on Carbon Surfaces as a Function of Temperature Using Molecular Dynamics. *Polymers* **2021**, *13*, 2162.

(68) Pineda, E. J.; Bednarcyk, B. A.; Ricks, T. M.; Arnold, S. M.; Henson, G. Efficient Multiscale Recursive Micromechanics of Composites for Engineering Applications. *Int. J. Multiscale Comput. Eng.* **2021**, *19*, 77−105.

(69) Pineda, E. J.; Ricks, T. M.; Bednarcyk, B. A.; Arnold, S. M. *Benchmarking and Performance of the NASA Multiscale Analysis Tool*; AIAA Scitech 2021 Forum: Reston, VA, 2021.

(70) Aboudi, J.; Arnold, S. M.; Bednarcyk, B. A. *Micromechanics of Composite Materials: A Generalized Multiscale Analysis Approach*; Elsevier, 2013.

(71) Aboudi, J.; Arnold, S. M.; Bednarcyk, B. A. *Practical Micromechanics of Composite Materials*, 1st ed.; Butterworth-Heinemann, 2021; p 416.

(72) Radue, M. S. Molecular modeling of aerospace polymer matrices including carbon nanotube-enhanced epoxy. Ph.D. thesis, Michigan Technological University, 2017.

(73) Thompson, A. P.; Aktulga, H. M.; Berger, R.; Bolintineanu, D. S.; Brown, W. M.; Crozier, P. S.; in 't Veld, P. J.; Kohlmeyer, A.; Moore, S. G.; Nguyen, T. D.; et al. LAMMPS - a flexible simulation tool for particle-based materials modeling at the atomic, meso, and continuum scales. *Comput. Phys. Commun.* **2022**, *271*, 108171.

(74) Plimpton, S. Fast Parallel Algorithms for Short-Range Molecular Dynamics. *J. Comput. Phys.* **1995**, *117*, 1−19.

(75) Stukowski, A. Visualization and Analysis of Atomistic Simulation Data with OVITO−the Open Visualization Tool. *Modell. Simul. Mater. Sci. Eng.* **2010**, *18*, 015012.

(76) Gissinger, J. R.; Jensen, B. D.; Wise, K. E. Modeling Chemical Reactions in Classical Molecular Dynamics Simulations. *Polymer* **2017**, *128*, 211−217.

(77) Gissinger, J. R.; Jensen, B. D.; Wise, K. E. REACTER: A Heuristic Method for Reactive Molecular Dynamics. *Macromolecules* **2020**, *53*, 9953−9961.

(78) MatWeb. Overview of materials for PETG copolyester, 2023. https://www.matweb.com/search/datasheet.aspx?matguid=4de1c85bb946406a86c52b688e3810d0{\&}cck=1.

(79) Pisani, W. A.; Jenness, G. R.; Schutt, T. C.; Larson, S. L.; Shukla, M. K. Preferential Adsorption of Prominent Amino Acids in the Urease Enzyme of Sporosarcina pasteurii on Arid Soil Components: A Periodic DFT Study. *Langmuir* **2022**, *38*, 13414−13428.

(80) Hjorth Larsen, A.; Jørgen Mortensen, J.; Blomqvist, J.; Castelli, I. E.; Christensen, R.; Dułak, M.; Friis, J.; Groves, M. N.; Hammer, B.; Hargus, C.; et al. The atomic simulation environment—a Python library for working with atoms. *J. Phys.: Condens. Matter* **2017**, *29*, 273002.

(81) Sorkin, V.; Pei, Q. X.; Liu, P.; Thitsartarn, W.; He, C. B.; Zhang, Y. W. Atomistic-scale analysis of the deformation and failure of polypropylene composites reinforced by functionalized silica nano-particles. *Sci. Rep.* **2021**, *11*, 23108−23114.

(82) Kanhaiya, K.; Kim, S.; Im, W.; Heinz, H. Accurate simulation of surfaces and interfaces of ten FCC metals and steel using Lennard−Jones potentials. *npj Comput. Mater.* **2021**, *7*, 17.

(83) Pilgrim, C. piecewise-regression (aka segmented regression) in Python. *J. Open Source Softw.* **2021**, *6*, 3859.

(84) Ha, H.; Thompson, R.; Hwang, B. Iron oxide layer effects on the sedimentation behavior of carbonyl iron powder suspension. *Colloids Interface Sci. Commun.* **2022**, *50*, 100670.

(85) Parveez, B.; Kittur, M. I.; Badruddin, I. A.; Kamangar, S.; Hussien, M.; Umarfarooq, M. A. Scientific Advancements in Composite Materials for Aircraft Applications: A Review. *Polymers* **2022**, *14*, 5007.

(86) Ghobadi, E.; Heuchel, M.; Kratz, K.; Lendlein, A. Simulating the Shape-Memory Behavior of Amorphous Switching Domains of Poly(L-lactide) by Molecular Dynamics. *Macromol. Chem. Phys.* **2013**, *214*, 1273−1283.

(87) Zhou, S.; Cheng, X.; Jin, Y.; Wu, J.; Zhao, D. Molecular dynamics simulation on interacting and mechanical properties of polylactic acid and attapulgite(100) surface. *J. Appl. Polym. Sci.* **2013**, *128*, 3043−3049.

(88) Li, X.; Xiao, T.; Xiao, N. The application of nonlocal theory method in the coarse-grained molecular dynamics simulations of long-chain polylactic acid. *Acta Mech. Solida Sin.* **2017**, *30*, 630−637.

(89) Glagolev, M. K.; Vasilevskaya, V. V. Coarse-grained simulation of molecular ordering in polylactic blends under uniaxial strain. *Polymer* **2020**, *190*, 122232.

(90) Alex, A.; Ilango, N. K.; Ghosh, P. Comparative Role of Chain Scission and Solvation in the Biodegradation of Polylactic Acid (PLA). *J. Phys. Chem. B* **2018**, *122*, 9516−9526.

(91) Ghobadi, E.; Heuchel, M.; Kratz, K.; Lendlein, A. Influence of the addition of water to amorphous switching domains on the simulated shape-memory properties of poly(l-lactide). *Polymer* **2013**, *54*, 4204−4211.

(92) Ghobadi, E.; Heuchel, M.; Kratz, K.; Lendlein, A. Influence of different heating regimes on the shape-recovery behavior of poly(L-lactide) in simulated thermomechanical tests. *J. Appl. Biomater. Funct. Mater.* **2012**, *10*, 259−264.

(93) Xiang, H.; Wang, Y.; Yang, W.; Hu, C.; Mu, Y.; Li, J. Study of the mechanical and thermal properties of poly(lactic acid) and poly(ethylene glycol) block copolymer with molecular dynamics. *Int. J. Polym. Anal. Charact.* **2010**, *15*, 235−244.

(94) McAliley, J. H.; Bruce, D. A. Development of Force Field Parameters for Molecular Simulation of Polylactide. *J. Chem. Theory Comput.* **2011**, *7*, 3756−3767.

(95) Sun, H. COMPASS: An ab Initio Force-Field Optimized for Condensed-Phase Applications Overview with Details on Alkane and Benzene Compounds. *J. Phys. Chem. B* **1998**, *102*, 7338−7364.

(96) Sun, H.; Jin, Z.; Yang, C.; Akkermans, R. L.; Robertson, S. H.; Spenley, N. A.; Miller, S.; Todd, S. M. COMPASS II: extended coverage for polymer and drug-like molecule databases. *J. Mol. Model.* **2016**, *22*, 47.

(97) Wang, X.; Zhao, L.; Fuh, J. Y. H.; Lee, H. P. Effect of porosity on mechanical properties of 3D printed polymers: Experiments and micromechanical modeling based on X-ray computed tomography analysis. *Polymers* **2019**, *11*, 1154.